Contents lists available at ScienceDirect

Journal of Molecular Liquids

Mixtures of ethylammonium nitrate and ethylene carbonate: Bulk and interfacial analysis

Raúl Lois-Cuns [a], Martín Otero-Lema [a], Alejandro Rivera-Pousa [a], Pablo Vallet [a], Juan J. Parajó [a], Oscar Cabeza [b], Hadrián Montes-Campos [a,c], Trinidad Méndez-Morales [a,*], Luis M. Varela [a,*]

[a] *Grupo de Nanomateriais, Fotónica e Materia Branda, Departamento de Física de Partículas, Universidade de Santiago de Compostela, Campus Vida s/n, E-15782, Santiago de Compostela, Spain*

[b] *Grupo Mesturas, Facultad de Ciencias, Universidade da Coruña, Campus da Zapateira s/n, E-15071, A Coruña, Spain*

[c] *CIQUP, Institute of Molecular Sciences (IMS)—Departamento de Química e Bioquímica, Faculdade de Ciências da Universidade do Porto, Rua Campo Alegre, 4169-007, Porto, Portugal*

ARTICLE INFO

ABSTRACT

The structure and dynamics of binary mixtures of a protic ionic liquid (ethylammonium nitrate) and ethylene carbonate are studied by means of atomistic molecular dynamics simulations and experimental measurements both in bulk and at the electrochemical interface. The solubility limit was experimentally found at 0.6 carbonate molar fraction. Likewise, density and conductivity experimental data are compared with computational results. Also, distribution and correlation functions obtained from bulk simulations are analyzed in the miscible range to clarify the role of the carbonate in the coordination and diffusion of ionic species. Understanding the evolution of the hydrogen bond network is of particular importance since its strength is detected as the most relevant feature in the structural organization of the mixture. Regarding the effects of the presence of an interface, the orientations of the molecules and the density and charge profiles are calculated both in the absence and in the presence of an electric field. This analysis reveals the tendency of the carbonate to displace the ionic liquid from the near-wall region when concentration is increased.

1. Introduction

The serious pollution problems our societies suffer nowadays have raised the interest of the international community in the development of new environmentally friendly technologies that lead to a more sustainable energetic model. Electrochemical energy storage devices have risen in popularity as a key piece in the renewable energy production as well as in electric vehicles. Despite the fact that conventional lithium-ion batteries have been successful up to now, they are no longer capable of meeting the current requirements in terms of capacity and security standards, as they usually rely on liquid organic electrolytes that are often highly flammable. As such, new types of electrolytes are being developed to alleviate the problems that lithium ion batteries present.

Ionic liquids (ILs), which are often defined as compounds consisting exclusively of ions with their melting point lying below 100 °C, have shown themselves to be promising candidates for this mission [1–3], since they present electrochemical and thermal properties suitable for

their use in energy storage [1]. ILs are usually made up of a bulky organic cation and an inorganic anion that present a strong asymmetry in their chemical structure, which allows them to remain liquid at room temperature [4]. A large number of possible anion-cation combinations that meet the previous condition exists and they show a wide range of useful properties, making it possible to create an IL for each specific application. Notwithstanding, there are some common characteristics among all the ILs, of which their low vapor pressure or high viscosity can be highlighted [5,6].

This last property is an obstacle when it comes to designing new energy storage devices, since it hinders ionic mobility within the electrolyte. Due to this, to reach the values of the ionic conductivity requested for many applications in the electrochemical industry, mixtures of ILs with different cosolvents that are able to reduce their viscosity (increasing ionic mobility) through the weakening of the electrostatic interactions of the system are being analyzed at the time. One type of cosolvent that can be included for IL customization are alkylcarbonates. These compounds, frequently used in commercially available lithium

---

* Corresponding authors.

E-mail addresses: trinidad.mendez@usc.es (T. Méndez-Morales), luismiguel.varela@usc.es (L.M. Varela).
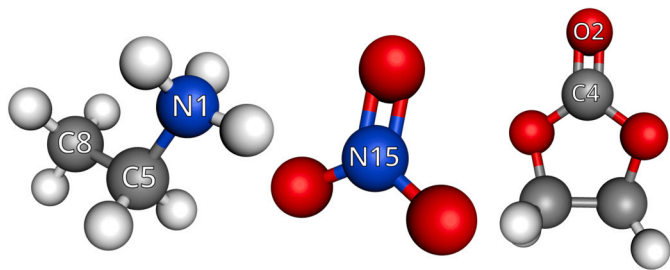
Fig. 1. Molecular structures of the different species in the system and names used for their most representative atoms. From left to right: ethylammonium, nitrate and ethylene carbonate. Red, blue, gray and white correspond to oxygen, nitrogen, carbon and hydrogen atoms, respectively.

batteries, are distinguished by the presence of the carbonyl group capable of modifying the structure of the IL by interacting with it. Thus, their mixtures have been analyzed both by experimental methods [7–21] and computational modeling [22–24]. For example, Linh et al. [7] proved experimentally that the addition of 20% of volume of ethylene carbonate (EC) decreases significantly the viscosity and improves the ionic conductivity of aprotic ILs at room temperature, reaching values similar to those obtained from conventional electrolytes based on organic solvents. Likewise, Vogl et al. [10] have shown similar effects using propylene carbonate as a cosolvent with protic ILs, reaching competitive values of conductivity and, depending on the amount of IL, such mixtures might also display the ability to suppress the anodic dissolution of Al.

Ternary mixtures including ILs, carbonates and alkali salts or molecular solvents such as water have also gained a lot of attention in recent years [25–34]. For example, Deshpande et al. [33] performed molecular dynamics (MD) simulations to analyze the transport and mobility of lithium ions in mixtures of N-methyl-N-propylpyrrolidinium bis(trifluoromethanesulfonyl)imide with EC and LiTFSI, among other carbonates. Thus showing that the addition of this organic solvent enhanced the self-diffusion of Li$^+$ and ionic conductivities (with increases up to 20% for a 0.2 EC mole fraction). On the other hand, by combining experimental measurements and MD simulations, Oldiges et al. [29] studied the influence of the amount of a pyrrolidinium-based IL in mixtures of EC/dimethyl carbonate (DMC) containing a lithium salt on the transport and solvation properties. They showed that an IL fraction of 10 wt% provides conductivity values comparable to those of industrially relevant carbonate-based electrolytes and, at the same time, it maintains the lithium transference numbers observed for standard electrolytes while noticeably improving their thermal and electrochemical stabilities.

However, it must be noted that computational approaches are still scarce even though they have proven valuable in providing a deep understanding of this kind of systems. Specifically, a full description at the molecular level of mixtures of EC with protic ILs, which are well-known for the presence of strong hydrogen bonds between the cation and the anion [35], has not been developed yet. Moreover, further studies regarding the microscopic structure of these systems are necessary to understand the different mechanisms operating within them. For that purpose, in this contribution MD simulations and experimental measurements were employed to analyze thermodynamic (density), structural (radial and spatial distribution functions and hydrogen bonds) and dynamic properties (velocity autocorrelation functions, self-diffusion coefficients and ionic conductivity) of ethylammonium nitrate (EAN) mixed with EC at different concentrations. Moreover, the computational analysis was extended to study the binary mixtures at the electrochemical interface (number density profiles, charge profiles and orientations), which is known to modify the properties of the bulk system [36], in order to test their potential as electrolytes for energy storage devices. The molecular structures of the ions and the additive are illustrated in Fig. 1.

The paper is structured as follows: in Section 2 we describe the details of the computational and experimental methodology, then in

Section 3 we present and discuss the results and, finally, in Section 4 we summarize our main conclusions.

2. Materials and methods

2.1. Experimental details

Ethylammonium nitrate, EAN(l), was purchased from IoLiTec with a stated purity (mass fraction) of 0.97. EAN sample was dried under vacuum for a minimum of 48 hours. The amount of water was less than 200 ppm, and it was measured by using a Karl Fisher titrator (Mettler Toledo C20), whose expanded uncertainty is 0.1 ppm. Ethylene carbonate, EC(s), was supplied by Acros Organics with a stated purity (mass fraction) higher than 0.99.

Density was measured by using a vibrating tube densimeter Anton Paar DSA 5000 at 298 K, with a resolution of 10^{-6} g · cm^{-3}. Apparatus calibration was performed with dry air and distilled water as previously described in Ref. [37].

Electrical conductivity was obtained with a sensION+ EC71 conductimeter from HACH, with a LZW 5292 probe formed by two parallel flat platinum plates, which can work in a temperature range from 243 to 323 K. Measurements were collected in a temperature range from 323 to 283 K. A calibrated Julabo F25 thermostat was used to control the temperature of the sample; the error in the temperature was lower than 0.1 K in the temperature range measured. These measurements were taken in an isothermal regime, so the time spent on each one was at least 15 min while there was no expected phase transition, around 310 K for EC [38] and 285 K for pure ethylammonium nitrate IL [39].

2.2. Computational details

Atomistic MD simulations of binary mixtures of EAN and EC were performed using the Groningen Machine for Chemical Simulations (GROMACS) version 2019.5 [40–42]. Also, the Optimized Potentials for Liquid Simulations in its all-atoms version (OPLS-AA) force field [43–45] was employed in all simulations. The parameters for the simulation of EC were extracted from Ref. [46], while the IL parameters have been already described in Ref. [47]. In those cases in which the mixtures are analyzed at the electrochemical interface, since we are not interested in the explicit interaction between the IL and the electrode surface, a planar interface was modeled using the option included in GROMACS for creating implicit walls instead of including a surface with real atoms. This effect is represented as a surface-integrated Lennard-Jones potential, so only the average of the interactions that those atoms would generate is taken into account. The atom type employed to represent the interaction was carbon opls_145 and the atomic wall densities were chosen to match that of graphene (38.18 atoms/nm^2). These implicit surfaces were placed at a fixed distance in the Z direction of 6 nm, which is large enough to allow the formation of a bulk-like central region that ensures the walls are not influencing each other [48]. In fact, this bulk-like region is expected to disappear with slit sizes smaller than 3 nm (depending on the IL), and the ionic distribution in the proximity of the interface is presumed not to show a dependence on the distance between walls. In this case, periodic boundary conditions were applied in X and Y directions only.

For all the systems, we started by creating a simulation box using PACKMOL [49], keeping the proper Z-length in the case of wall simulations. Different simulation boxes were created for each concentration, ranging from pure EAN to 60 mol% EC and always keeping a total of 1000 molecules in the simulation box. Thus, 50% entails 500 ionic pairs and 500 molecules of EC. Simulations beyond 60% EC were not carried out, since it was found experimentally that the system is not miscible for higher concentrations, as will be discussed below. In bulk simulations, for which full three-dimensional periodicity was applied, the creation of the box was followed by an energy minimization using a conjugate gradient algorithm with a 0.1 kJmol^{-1} nm^{-1} tolerance. After that a 20 ns
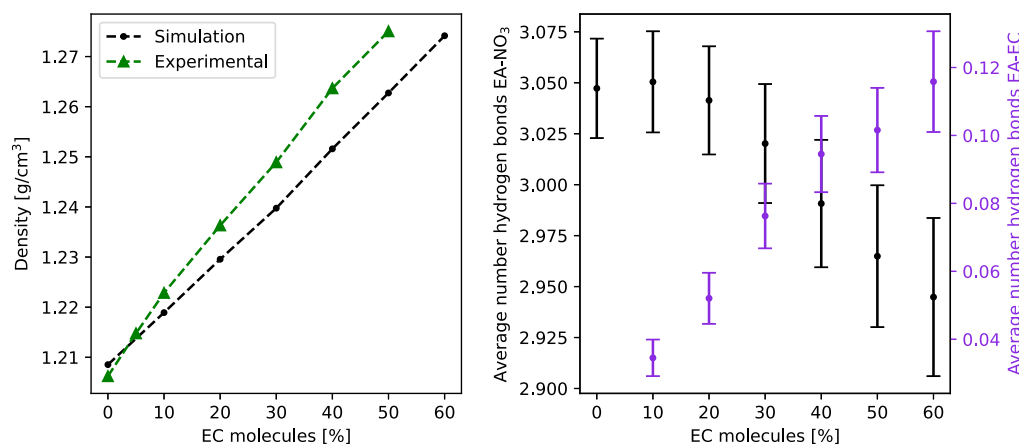
Fig. 2. Left: simulated (circles) and experimental (triangles) densities at $T = 298.15$ K for different concentrations. Expanded standard uncertainties are 0.0050 g/cm^3 (0.95 level of confidence) for experimental data. Relative statistical uncertainties of computational density data are less than a 0.001%. Dashed lines are included as a guide to the eye. Right: average number of cation-anion (black) and cation-cosolvent (purple) hydrogen bonds per cation.

stabilization in the NpT ensemble (298.15 K and 1 atm) was carried out using a 2 fs timestep. Finally, a single production run of the same length was carried out for each concentration to obtain the structural properties. For the calculation of the dynamic ones, extensions to these simulations were performed. In particular, for the calculation of the velocity autocorrelation functions, new 250 ps runs with a 1 fs time step were carried out, recording velocities at each simulation step. For the computation of the conductivity extended 40 ns NVT simulations (with a timestep of 1 fs) were carried out, with velocities also being recorded at each step.

On the other hand, for neutral wall simulations the energy minimization was carried out using a steepest descent algorithm with the same tolerance as the previous ones, as it is more consistent in the first steps of the minimization. After this a first 13 ns stabilization in the NpT ensemble (298.15 K and 1 atm) was carried out, where the first 3 ns included an annealing process to avoid metastable configurations. This treatment involved a linear increase in the temperature up to 600 K and then a decrease back to the production temperature. In this case the timestep was reduced to 1 fs. Then, a 10 ns NVT stabilization and a 20 ns NVT production run, both with a 2 fs timestep, were performed. For charged wall simulations, the effect of charges on the electrode surface was mimicked by adding a constant electric field in the Z direction. Starting from the last configuration obtained in the neutral wall simulations for each concentration, a 18.18 V/nm electrostatic field was included between the walls, which corresponds to a charge density of ± 1 e/nm^2 in each wall. Then, a 10 ns NVT stabilization with a 1 fs timestep was carried out followed by a 20 ns production run with a timestep of 2 fs.

Long-range Coulomb interactions were computed using the smooth Particle-Mesh Ewald electrostatics method [50] with a real space cut-off radius of 1.1 nm. The Fourier grid spacing was 0.12 nm with cubic interpolation. Verlet cutoff scheme was employed to allow the optimization of grid spacing and Coulomb cut-off. The Linear Constraint Solver (LINCS) algorithm [51,52], with a fourth order expansion of the constraint coupling matrix was used to fix all the bond lengths with H-atoms. Moreover, for wall simulations the Yeh-Berkowitz correction [53] was applied for the calculation of the Coulomb interaction. Finally, van der Waals forces were considered within a cut-off radius of 1.1 nm. Temperature was controlled by means of the V-rescale thermostat (0.1 ps coupling constant), which includes a stochastic term to ensure a proper canonical ensemble [54]. Pressure was kept constant by employing an isotropic Parrinello-Rahman barostat [55] for bulk simulations, and a semi-isotropic pressure coupling for the ones with implicit walls (1 ps coupling time).

3. Results and discussion

3.1. Bulk simulations and experimental results

The first step was the determination of the solubility of EC (solid at room temperature) in EAN (liquid), since no information has been found about EC-EAN solubility. Different molar fractions of the mixture were prepared at room temperature. Beyond an 80% of EC it was directly observed that the mixture was not fully soluble. The rest of the mixtures were kept for 48 hours in order to see possible precipitation, or two phases formation. After this time it was found that the maximum solubility was reached at a 60% of EC molecules at room temperature.

3.1.1. Density and hydrogen bonds

Some information on the structural effect of EC addition to EAN can be obtained from the analysis of volumetric properties. The comparison between computational and experimental densities of the system for different EC concentrations at room temperature are shown in Fig. 2. Even though the solubility limit was found at a 60% concentration of EC, experimental measurements were carried out up to a lower concentration in order to avoid any damage of the apparatus. A monotonic increase with EC concentration is registered, as expected due to the higher density of the carbonate. As it can be seen, the agreement between computational and experimental data is excellent in the low cosolvent concentration range. Moreover, both values for pure EAN are in good agreement with previously reported measurements [37,56]. These results are further apart in the region near the immiscible regime where the computational predictions are slightly underestimated, but the difference between both methodologies is always less than 1%. These deviations are clearly below the 5% threshold usually accepted to validate numerical simulations. Both data sets are included in Table S1 of the Supporting Information.

In order to make a first approach towards the microscopical behavior, the hydrogen bonds between the various species in the mixture can be calculated. This can be done in two ways, using either energetic or geometrical criteria for the definition of what is a hydrogen bond [57]. Regarding the latter, two molecules are considered to form a hydrogen bond if the distance between the donor and the acceptor is less than 0.35 nm and the angle hydrogen-donor-acceptor is less than 30°. In this work the NH groups of the cation will be considered as donors and the O of the anion and cosolvent as acceptors. Thus, in Fig. 2 the average number of hydrogen bonds normalized to the number of cations (donors) in the system is shown for both cases of cation-anion and cation-cosolvent bonds. As can be seen, from the well-known result of three hydrogen bonds formed by pure EAN [58] a slight decrease in the average number of hydrogen bonds is obtained when the carbonate concentration
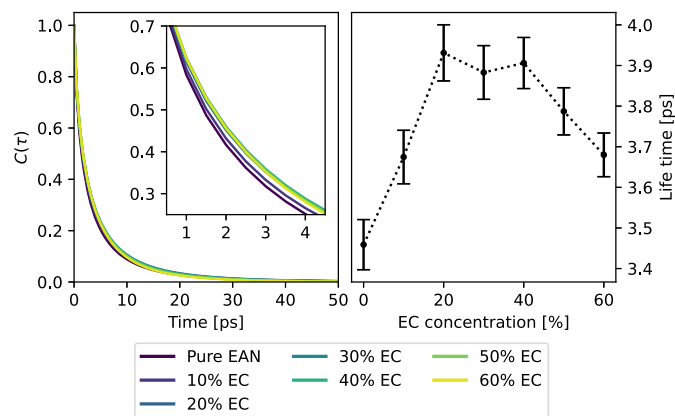
Fig. 3. EC concentration dependence of (left) the time autocorrelation functions of the presence of a cation-anion continuous hydrogen bond, and of (right) the cation-anion hydrogen bond lifetimes. Error bars are calculated from the results of fitting the biexponential described in [59].

is increased, due to the formation of new cation-cosolvent hydrogen bonds. In any case, it can be stated that the presence of EC does not lead to any considerable disruption of the hydrogen bond network of the bulk IL for low carbonate concentrations (until 20% EC). For higher concentrations its interaction with the IL is not relevant either, only resulting in a disruption of less than 4% for concentrations near the solubility limit.

To further analyze the evolution of the three-dimensional network of hydrogen bonds characteristic of EAN, we computed the time autocorrelation function of the presence of a hydrogen bond as

$$C(\tau) = \left\langle \frac{h_{ij}(t_0)h_{ij}(t_0 + \tau)}{h_{ij}^2(t_0)} \right\rangle, \tag{1}$$

where h_{ij} indicates the presence of a hydrogen bond between atoms i and j and takes the values 1 or 0 if there is or not a hydrogen bond, respectively. In our calculations both intermittent and continuous hydrogen bonds were considered, where the intermittency argument indicates the maximum number of frames for which a hydrogen bond is allowed to break and then being re-formed and counted again at a future point in time. An intermittency of zero is equivalent to a continuous hydrogen bond, which means that if a hydrogen bond is not present at any frame between t_0 and $t_0 + \tau$ it will be considered as missing at $t_0 + \tau$. The comparison of the intermittent hydrogen bonding time autocorrelation functions for several intermittencies and different EC concentrations is included in Fig. S1 of the Supporting Information. Additionally, in Fig. 3 the continuous hydrogen bonding time autocorrelation function (left) is included together with the hydrogen bond lifetime (right) as a function of EC concentration, which was calculated as described in Ref. [59]. It can be seen that there is little variation of the hydrogen bond lifetime value with the addition of EC to the system, which is compatible with the abovementioned weak disruption of the network.

3.1.2. Radial distribution functions and coordination numbers

To study in more detail the microscopic interactions between the components of the system, the radial distribution functions (RDFs) were calculated. From them, the cumulative radial distribution functions (CRDFs) were also computed in order to evaluate the coordination numbers. Both functions can be obtained from the simulation trajectories as

$$\mathrm{RDF}_{ab}(r) = \frac{V}{N_a N_b} \sum_{i=1}^{N_a} \sum_{j=1}^{N_b} \frac{\langle \delta(r_{ij} - r) \rangle}{4\pi r^2}, \tag{2}$$

$$\mathrm{CRDF}_{ab}(r) = \frac{N_b}{V} \int_0^r 4\pi r'^2 \mathrm{RDF}_{ab}(r') dr', \tag{3}$$
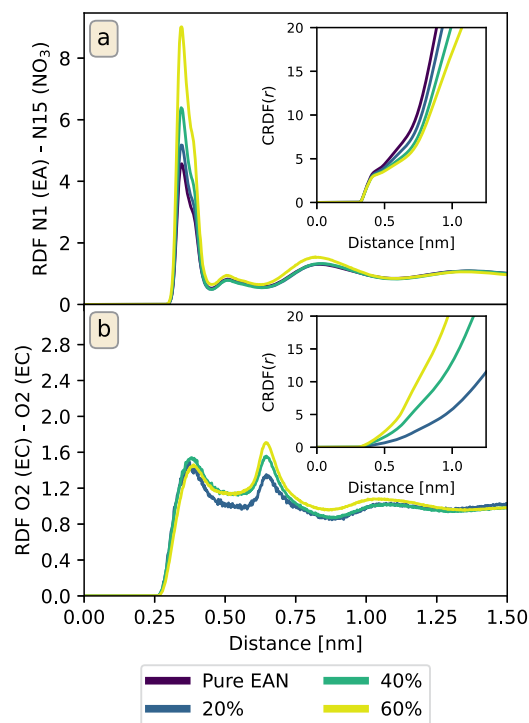
Fig. 4. RDFs for the cation-anion (top) and the cosolvent-cosolvent (bottom) interaction. Insets represent the CRDFs.

respectively. In the above equations N_i represents the number of particles of species i, V the volume and brackets indicate the ensemble average. From the CRDF the coordination number (CN) of b species surrounding a can be defined as $\mathrm{CRDF}_{ab}(r_0)$ with r_0 corresponding to the distance of the first solvation shell of a, *i.e.*, the first minima of the RDF. For the RDF calculations different atoms were considered in each case: the nitrogen atom (N15) of $[NO_3]^-$, the nitrogen atom (N1) and the carbon in the ethyl group (C8) of $[EA]^+$ and the carbonyl oxygen atom (O2) of EC. All of them are labeled in Fig. 1.

The analysis of the RDF of the anion-cation interaction (Fig. 4a) shows that the structure of the pure IL is not strongly modified when EC is added to the system and no changes in the solvation distances are found. The main modification is the increase in the height of the first peak as increasing the amount of carbonate that indicates a tendency of the IL to form clusters. Similar behavior was found in previous studies with EAN in mixtures with other polar solvents as methanol [47] or dimethyl sulfoxide [60]. But in contrast with these works, no significant interaction of the IL with the EC is found as it can be seen in the RDFs of the nitrogen atoms of the ions (Fig. 5a and 5b), which represent the most interacting regions of these molecules. No relevant adsorption points of EC appear near these nitrogen atoms at low EC concentrations and, when concentrations near the immiscible regime are approached, all these nearby adsorption regions end up disappearing.

To understand what happens with the cosolvent, the RDFs for the carbonate molecules were also determined. The height of the peaks in Fig. 4b indicates weak interactions between solvent molecules, which are well integrated in the mixture and do not tend to form aggregates. This is consistent with previous findings in mixtures of EC with a pyrrolidinium-based IL doped with a lithium salt [34]. It is also useful to study the RDF of the tail of the $[EA]^+$ with the carbonyl oxygen of the EC (Fig. 5c). As it can be seen, the coordination of EC with the ethyl group of the cation is more probable than with its polar head, revealing that this solvent prefers the least charged parts of the ions. In short, EAN is characterized by a pronounced polar–apolar domain segregation and it was observed that the inclusion of EC in the system is not capable of breaking the three-dimensional hydrogen bond network formed
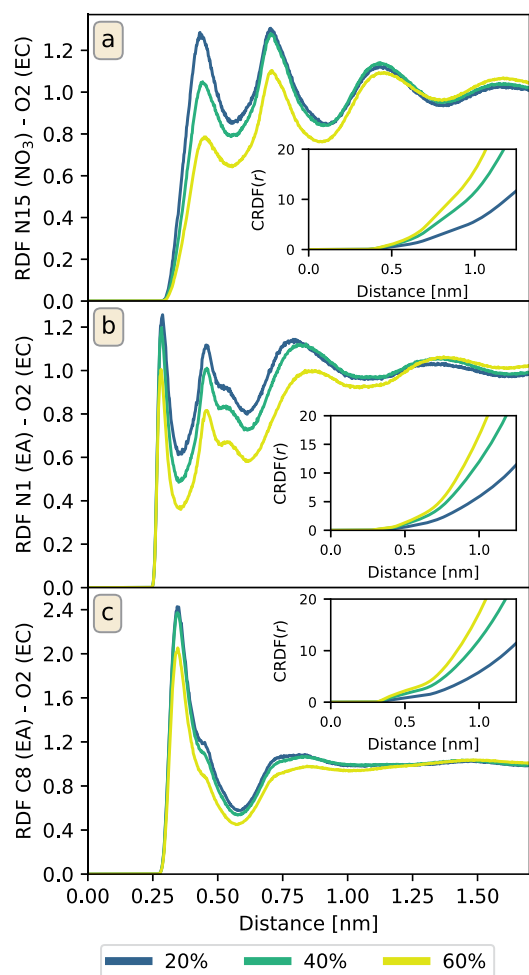
Fig. 5. RDFs for the anion-cosolvent (a) and the cation-cosolvent (b and c) interaction. Insets represent the CRDFs.

Table 1
Coordination of the different atoms showed in Fig. 4 and 5 for different EC concentrations (showed in the top row). The distance employed for the calculation is included in parentheses for each pair of atoms.

	0%	10%	20%	30%	40%	50%	60%
N1 - N15 (0.452 nm)	3.77	3.64	3.49	3.41	3.31	3.25	3.24
O2 - O2 (0.590 nm)	-	0.61	1.17	2.02	2.74	3.47	4.25
N15 - O2 (0.544 nm)	-	0.36	0.73	1.02	1.30	1.50	1.57
N1 - O2 (0.358 nm)	-	0.06	0.14	0.19	0.26	0.31	0.32
N1 - O2 (0.598 nm)	-	0.50	1.04	1.48	1.95	2.32	2.47
C8 - O2 (0.598 nm)	-	0.58	1.17	1.75	2.34	2.83	3.10

by this IL. The features of the RDFs support the image of EC embedded in the nanostructured protic IL and, as its concentration increases, carbonate aggregation will be more relevant until reaching the solubility limit where large heterogeneous regions are generated.

The coordination numbers derived from the RDFs and the CRDFs in Figs. 4 and 5 are given in Table 1. They confirm the weak influence of EC in the structuring of the ionic species, since their coordination numbers do not vary significantly upon increasing the amount of solvent. Near the solubility limit, the first shell of the cation is increasingly shared between nitrates and carbonates, although the latter is placed at slightly longer distances. However, for these amounts of solvent, a crossover from anion-based cation coordination to a carbonate-based coordination is not observed.
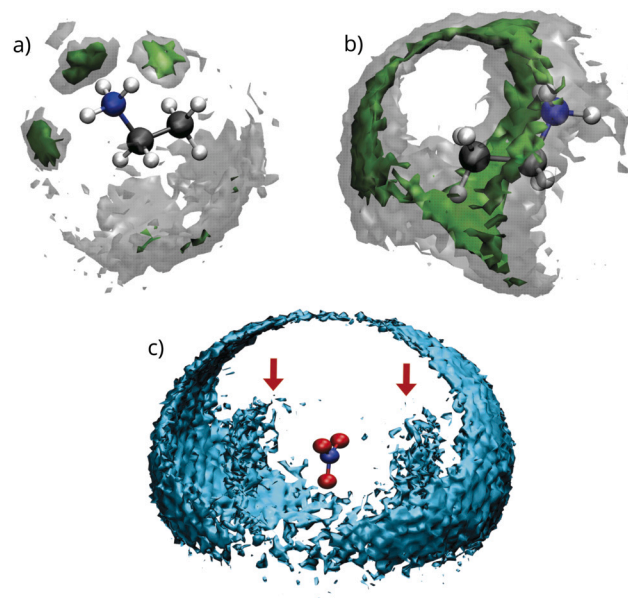

Fig. 6. Spatial distribution functions of ethylene carbonate around the cation (top) and the anion (bottom) for a 40% concentration of solvent. Green and transparent isosurfaces in (a-b) and cyan isosurface in (c) represent the regions with a probability of finding an EC molecule 4.0, 2.5 and 1.5 times greater than the probability of an homogeneous distribution, respectively, determined by the carbonate bulk density. The red arrows in (c) have been included with the purpose of highlighting the inner solvation shell of EC molecules around the anion.

3.1.3. Spatial distribution functions

In order to obtain a three-dimensional picture of the structural distribution of the carbonate around the ions in the bulk, the spatial distribution functions (SDFs) were calculated, i.e., the angular dependence of the probability distribution of finding a particle at a given distance from another one. Different isosurfaces of numerical density of the carbonyl oxygen atoms of the EC surrounding both ions were computed using as reference: the three hydrogen atoms bonded to the nitrogen in [EA]$^+$, the ones bonded to C8 carbon atom of [EA]$^+$ and the three oxygen atoms in [NO$_3$]$^-$. In Fig. 6 the results for a concentration of 40% EC are shown, but they are analogous for any other value of the concentration of carbonate. As it can be seen, the carbonate is placed forming two solvation shells around the anion, in perfect agreement with what was observed in Fig. 5. The prevalent position of EC on this solvation shell is in the region directly over nitrogen or in the bisectrix of the angle formed by two oxygen atoms and the central nitrogen, thus leaving the areas in direct contact with this atoms for the coordination between the anion and the cation. On the other hand, the SDFs around the cation confirm that carbonate molecules are preferentially adsorbed in the area close to the cation tail instead the one near its polar head. It is interesting to note the great contrast between these two regions: whereas in the polar head the EC prefers to be accommodated facing the hydrogen atoms (thus breaking the hydrogen bonds with the [NO$_3$]$^-$), in the apolar tail of the cation the carbonate molecules are located in the regions surrounding the hydrogen atoms but avoiding direct contact with them.

3.1.4. Diffusion and conductivity

To analyze the dynamic properties of a system, correlation functions are generally used, as they measure the degree of relationship between the dynamic variables at different times. Specifically, the velocity autocorrelation functions (VACFs) can be used for studying the single-particle dynamics of these mixtures, which can be computed as

$$\text{VACF}_i(t) = \langle \mathbf{v}_i(t + t_0)\mathbf{v}_i(t_0) \rangle, \qquad (4)$$
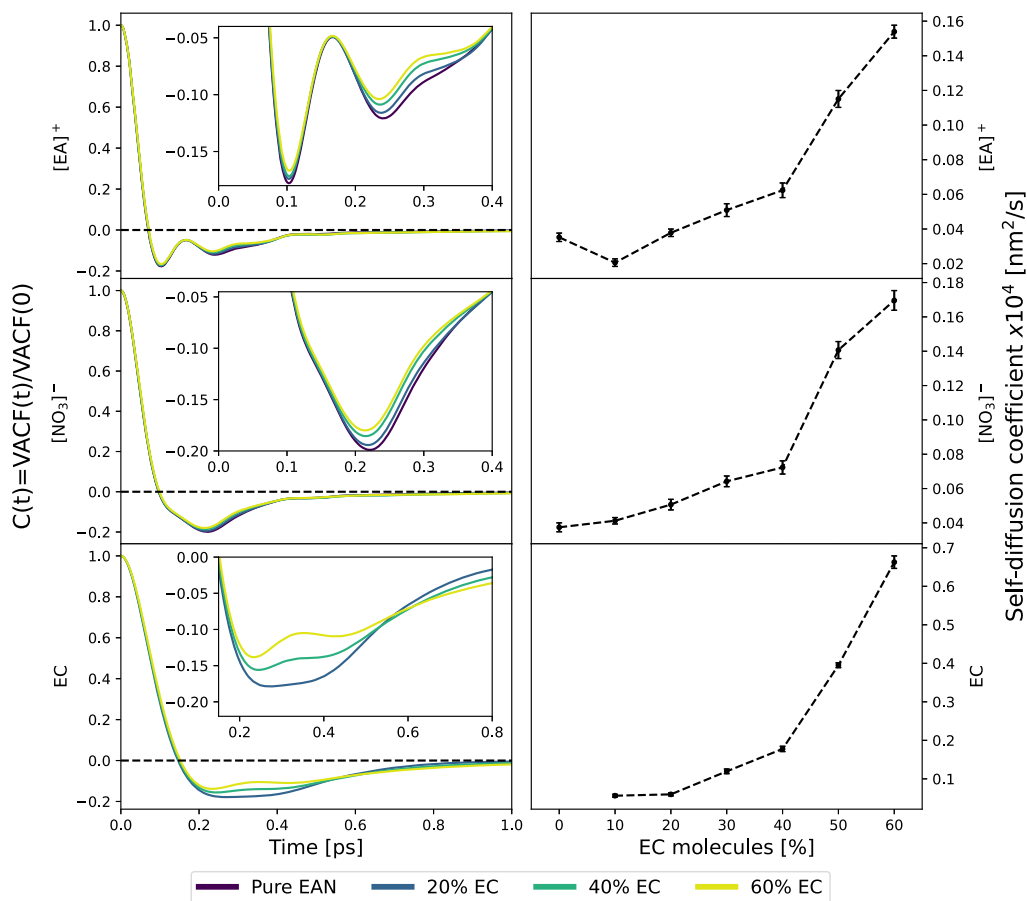
Fig. 7. Normalized VACFs of the different species (left) and their self-diffusion coefficients (right) as a function of solvent concentration. Dashed lines are a guide to the eye. From top to bottom: cation, anion and carbonate. The insets show a zoom around the minimum of the VACFs.

where the brackets correspond to the time average over all the particles of species i within the system and all possible time origins.

A normalized version of the VACFs of the center of mass of all species in the system is shown in Fig. 7. Consistently with what is observed when studying the structure of the system, the addition of cosolvent does not significantly modify the shape of the VACFs of the ions or their decay-to-zero time.

Thus, as in the case of pure EAN, $[NO_3]^-$ dynamics is shown to be bound to those of the cation, which is reflected in the fact that both species exhibit a similar decay-to-zero time. However, whereas the VACFs of the anion monotonically vanish, those of the cation undergo an oscillation before asymptotically vanishing. This is indicative of anions having a collision with another molecule before they rebound from one another and diffuse away, and cations experiencing a very weak cage effect. To illustrate this cation-anion behavior and the cage effect that is induced in the cation, cage autocorrelation functions (CaCF) of the ionic pair are included in Fig. S3 of the Supporting Information. These ion cage autocorrelation functions have been computed following the procedure described in Ref. [60], with a cutoff distance of 0.452 nm that corresponds to the first cation-anion solvation shell, and they show the presence of relatively resilient cages that become weaker with the addition of EC. Moreover, the $[EA]^+$ dynamics is more influenced by the presence of EC, as can be seen by the small changes in its second valley when increasing the concentration. This is associated to the fact that EC molecules are mainly accommodated in the surroundings of EAN, enhancing ionic motion. Finally, a more remarkable change is found in the VACF of the carbonate when varying the concentration. In this case, the VACF evolves from a smooth behavior for low concentrations related to a weak interaction with the ionic pairs, to an enhanced rattling motion at higher concentrations due to the interactions with other

EC molecules in the mixture. Also it is interesting to see that, in contrast with the ions, which are trapped in their solvation shells during 0.4 ps before escaping to the bulk, EC molecules enter this regime after 0.7 ps, due to their different sizes.

In addition, the vibrational Density of States (vDOS) can be straightforwardly obtained, since it is directly related to the Fourier transform of the VACFs. The results for the three species as a function of EC concentration are included in Fig. S2 of the Supporting Information, where the spectrum of the carbonate shows a slight decreasing of the peak at low frequencies in favor of the appearance of a shoulder at frequencies around $100\,cm^{-1}$ when increasing the amount of carbonate.

The self-diffusion coefficients can be obtained from the VACFs using the conventional Green–Kubo relation:

$$D_i = \frac{1}{3} \int_0^\infty VACF_i(t)dt. \tag{5}$$

The above integral can be numerically estimated by calculating the cumulative integral and averaging when it starts to oscillate around a defined value, which can be established after 50 ps. To carry out this average and to be able to determine an uncertainty, this interval was divided in 10 fragments, the self-diffusion coefficient and its uncertainty being the average of the mean values of each segment and their standard deviation, respectively.

These results are shown in the right column of Fig. 7, where it can be seen that at low concentrations, up to a 20% of EC, there is hardly any growth in the self-diffusion coefficients, and even a decrease can be seen in the case of $[EA]^+$ for 10% cosolvent concentration in the mixture. For higher amounts of carbonate, an enhancement of self-diffusion of all species is obtained, as expected from previous works
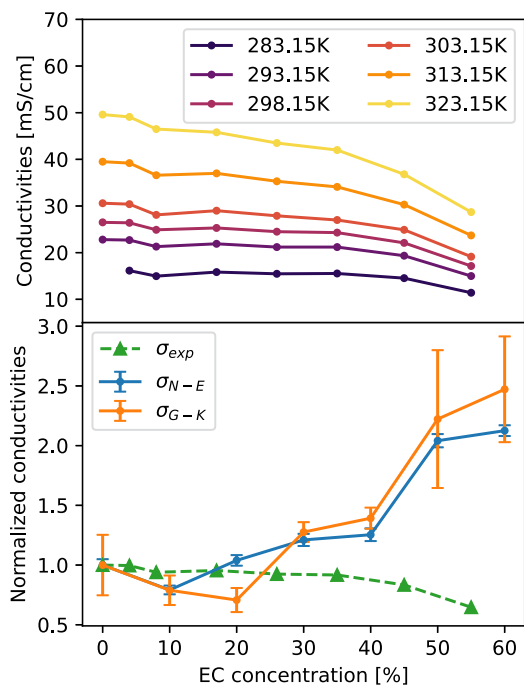
Fig. 8. Experimental conductivities as a function of EC concentration (as mole percentage) measured for different temperatures (top). Comparison between the experimental conductivity values and those obtained in the simulations both at $T = 298.15$ K (bottom). Expanded standard uncertainties for experimental conductivities are 1.0 mS/cm (0.95 level of confidence). In both figures lines are included as a guide to the eye.

of mixtures with carbonates [26,29,33,34]. This increase is linked, as can be seen when comparing with Fig. 2, to the weakening of the hydrogen bond network and the consequent reduction of the viscosity of the sample, thus favoring ionic motion. Finally, it should be noted that when approaching the solubility limit (around 50% EC) the growth of the self-diffusion coefficient becomes more abrupt. This is probably due not only to macroscopic effects linked to reduced viscosity, but also to a higher level of clustering that causes the ionic complexes to move together as a recognizable kinetic entity, as it can be seen in Fig. S3 where, even for the highest amount of carbonate, around a 20% of the cations are still surrounded by the same anions as at the beginning. Indeed, the enhancement of ion self-diffusion coefficient from pure IL up to carbonate saturation is around a factor of 4 in both cases. These observations concerning the diffusion of the three species can be also made by analyzing their mean squared displacements (MSDs), which are included in Fig. S4 of the Supporting Information as a log-log plot for several EC concentrations.

Fig. 8 (top) shows the experimental curves of the variation of the ionic conductivity with the amount of carbonate at different temperatures, as well as a comparison with the computational data at 298.15 K (bottom). Values of the experimental data sets are included in Table S2 of the Supporting Information. From the experimental measurements it can be seen how EC molecules do not increase the conductivity of EAN over the studied solubility range. Measured pure EAN conductivity values are in complete agreement with previously reported results [37,56]. To the best of our knowledge, no conductivity data of these systems can be found in the literature, although mixtures of EAN with other solvents have been published, such as its mixture with water [56,61], nitromethane [62] and dimethyl carbonate [63], among others. In most cases, the introduction of different amounts of aqueous and non-aqueous solvents into an IL leads to an increase in ionic conductivity (in contrast to the addition of a salt) due to the increase in ion mobility. However, EAN has been found to show a significant degree of ionic association and, as it was observed in the structural analysis, EC

is not able to liberate ions from their aggregates up to concentrations close to saturation, when the strong hydrogen bond interaction between anions and cations is replaced by strong intermolecular interactions between carbonates and cations. It must be taken into account that this non-coordinating role of EC would probably limit the ion transport number in case of adding a salt to the system. This behavior has been previously observed experimentally for pyrrolidinium nitrate-based ILs [19] in mixtures with propylene carbonate. Concerning the temperature dependence, it can be seen that the ionic conductivity of each composition increases with the temperature, as expected.

The experimental values obtained for the conductivity of the system can be compared with the results of MD simulations. Specifically, the conductivity can be computed from the self-diffusion coefficients obtained from the VACFs using the Nernst-Einstein (NE) relation:

$$\sigma_{N-E} = \frac{Ne^2}{k_B T V}(D_{\text{EA}} + D_{\text{NO}_3}), \tag{6}$$

where N stands for the ion number for each concentration. However, although this relationship has proven to be useful for concentrated mixtures, its use should be restricted to diluted systems as this relationship neglects all possible correlations between the ionic species. As in this work only high ionic concentration systems are analyzed, Green-Kubo (GK) relations are also useful for estimating the conductivity. These relations, which take into account this ion correlation, state that for homogeneous and isotropic systems the conductivity of the system can be related to the current autocorrelation function (CACF) through:

$$\sigma_{G-K} = \frac{1}{3k_B T V} \int_0^\infty \text{CACF}(t)dt = \frac{1}{3k_B T V} \int_0^\infty \langle \mathbf{j}(t_0 + t) \cdot \mathbf{j}(t_0) \rangle dt, \tag{7}$$

where $\mathbf{j}(t)$ is the total current of the system at time t. From the velocities of the extended simulations already mentioned in Section 2, the total current was computed using GROMACS. Then, the autocorrelation was computed and its uncertainty calculated from the proper definition of the variance. From these results, the integral was estimated using the composite trapezoidal rule and its uncertainty following usual uncertainty propagation rules. Finally, the weighted average of the results of this integral from 0.1 *ns* to the last lags of the correlation were used to obtain the value of the conductivity. It was found that the cumulative integral had stabilized around its average value for this lag choice. Small deviations on this choice of averaging time were found to not alter the conductivity value up to the statistical uncertainty.

The comparison between the experimental conductivity at $T = 298.15$ K and the computational values obtained by using the NE relation and the GK methodology is plotted in Fig. 8. For the sake of clarity, all the measurements have been normalized by their values for pure EAN, which for NE and GK are (3.03 ± 0.15) mS/cm and (0.64 ± 0.16) mS/cm, respectively. As expected, our computational results are lower than the experimental one by around one order of magnitude, since the force field employed is not polarizable and thus it suffers from slow dynamics [64,65], although it has been observed to predict the dynamics of ionic species qualitatively well [66,67]. However, the use of non-polarizable force fields for structure calculations, which are the main objective of this work, is well established and presents good results. As can be seen in the figure, when low/medium amounts of EC are added to the system, the simulations reveal no remarkable changes in the ionic conductivity, which is consistent with the experiments and with the previous structural findings of carbonate molecules not introducing significant changes in the ionic environment and, instead, accommodating themselves in the intermolecular voids. On the other hand, when the mixture is close to saturation, MD simulations show an increase in the ionic conductivity despite the lower amount of ions per volume under dilution, which is due to a decrease in the viscosity and the greater diffusion of ions reported in Fig. 7 and is in line with previous computational predictions [34]. Both NE and GK methodologies reproduce the same behavior as a function of carbonate
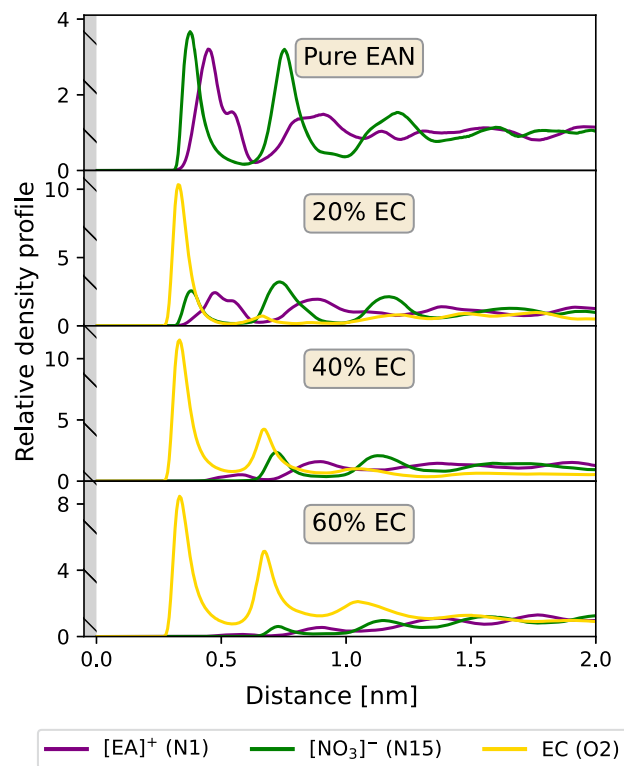
Fig. 9. Density profiles, normalized to the bulk density, for each species of the mixture in the proximity of a neutral surface as a function of EC concentration.

concentration, but the former are higher because this relation neglects the cross-correlations of the single particle velocities, due to which a pair of ions with opposite charges would contribute to the diffusion but not to the conductivity, thus leading to a decrease in this magnitude.

### 3.2. Interfacial simulations

3.2.1. Density profiles

With the aim of gaining some insight on the reorganization of the mixture at the electrochemical interface, wall simulations were performed as described in Section 2. Firstly, the density profiles of the system were calculated, i.e., the number density of the different particles of the system on the z-axis. It must be noted that the density profiles computed here are calculated taking one atom as reference for each species: the nitrogen of the ions and the carbonyl oxygen atom of the EC. Normalized density profiles for the neutral walls systems are shown in Fig. 9 for several concentrations of carbonate. Bulk density was computed as the mean value of the region between 2.0 nm and 4.0 nm. Only the results for the surface located at z = 0 are represented in Fig. 9, but the results for the opposite one are completely analogous, as expected. As it can be seen, the well-known electrical double layers (EDLs), that are typically found in these kinds of ionic systems [68–70], are present. These layers can be clearly observed in the case of pure EAN where oscillations in the distribution functions are observed fading away into the bulk densities near the walls. The addition of carbonate to the system displaces the ionic species from the region closer to the walls towards the center of the simulation box, showing a stronger affinity for the carbon surface than the IL. Indeed, when increasing EC concentration a larger number of EC layers are observed near the walls, e.g., at 40% concentration a second layer can be seen at 0.70 nm from the wall, which had just started to form at 20% concentration. At the same time, a vanishing of the ionic layers can be seen at the highest concentration in the regions closer to the walls, where the ionic concentration is lower than the bulk one. This effect of EAN being restricted to the center of the box could be indicative of a segregation between the IL and

the carbonate due to the presence of the walls, which induces a solubility limit at lower concentrations than in the bulk. It can also be noted the existence of an inversion of the ionic species closest to the wall once the second layer of EC at 0.70 nm is formed, with the cations being the closest to the wall instead of the anions (as observed for pure EAN). A possible explanation could be found in the fact that cations interact to a greater extent with EC, as it was observed when analyzing the bulk, so they go along with solvent molecules when they place themselves in the neighborhood of the surface, thus generating this change in the ionic ordering. Finally, it can be also highlighted that the height of the second peak for EC density profiles increases with increasing solvent concentration up to 5 times higher than the bulk density. This is even accompanied by the appearance of a third layer further away from the wall (around 1.1 nm) when approaching the solubility limit; whereas the height of the first peak shows the opposite behavior.

Density profiles, normalized to the bulk density for charged walls (computed using the same criteria as for neutral wall simulations), are shown in Fig. 10. In this case, the profiles of the main carbon of the carbonyl group have been included since, as it is discussed below, the orientation of the molecules will be of vital importance to understand charge distribution in the system. Firstly, looking at the positive wall (placed at $z = 0$ nm) it is immediate to see how, even though the inclusion of EC changed the distribution of ions in the mixture near the neutral interfaces, in this case the relative distance of $[NO_3]^-$ to the wall does not change and it remains in the region adjacent to the surface. However, the relative density of $[NO_3]^-$ in the vicinity of this positive wall with respect to that in the bulk decreases with the addition of carbonate to the system, as expected. With regard to the cation, increasing EC concentration leads to a displacement of $[EA]^+$ from a nearby region to the anion to a region at approximately 0.8 nm and at lower density than in the bulk. This is due to the preferential attachment of the carbonate close to the surface (at approximately the same distance as the anion), which replaces the cation by cosolvent molecules at the interface. At the highest EC concentration, we can observe an ionic layering behavior that is compatible with classical Stern model of the electric double-layer, since only one layer of anions completely screens the field.

On the other hand, the situation at the negative surface (at $z = 6$ nm) is very different. At low concentrations, it can be seen how the polar head of $[EA]^+$ (with a positive net charge) is located at the vicinity of the wall, barely allowing the carbonate to be located in this region (see Fig. 10 for 20% EC). As EC concentration is increased, more carbonate is located close to the wall, leading to the formation of EC barriers around this negative surface. At moderate EC concentrations, $[EA]^+$ molecules are still able to cross these formations, their maximum concentration value being at the same distance in which they would be found in pure EAN. However, as EC concentration approaches the solubility limit, the cation is replaced by carbonate molecules and carbonate layers are formed at 1 nm from the wall. This leads to the formation of several layers of cations and anions in the region between 4 and 5 nm for high EC concentrations, as the cations (and the group of anions to which they are bound) are restricted to be in this region before the new EC barrier. This behavior is completely different from that observed near the positive electrode. A suitable explanation for these distinct behaviors between the positive and negative carbon structures lies on the different sizes of the ions. As the $[NO_3]^-$ molecules have a considerably smaller size than those of $[EA]^+$ and EC, they can cross the layer formed by the carbonate, both species being mixed up and located at the same distance from the positive wall. However, $[EA]^+$ is not able to cross this barrier towards the negative surface for high concentrations of EC, the situation where it is behind this barrier being more favorable, and thus prevailing the affinity of EC for accommodating itself close to the wall over the effect of the field. We expect that, increasing the strength of the electric field, a larger amount of EC would be necessary to completely displace the ionic species from the region next to the wall.
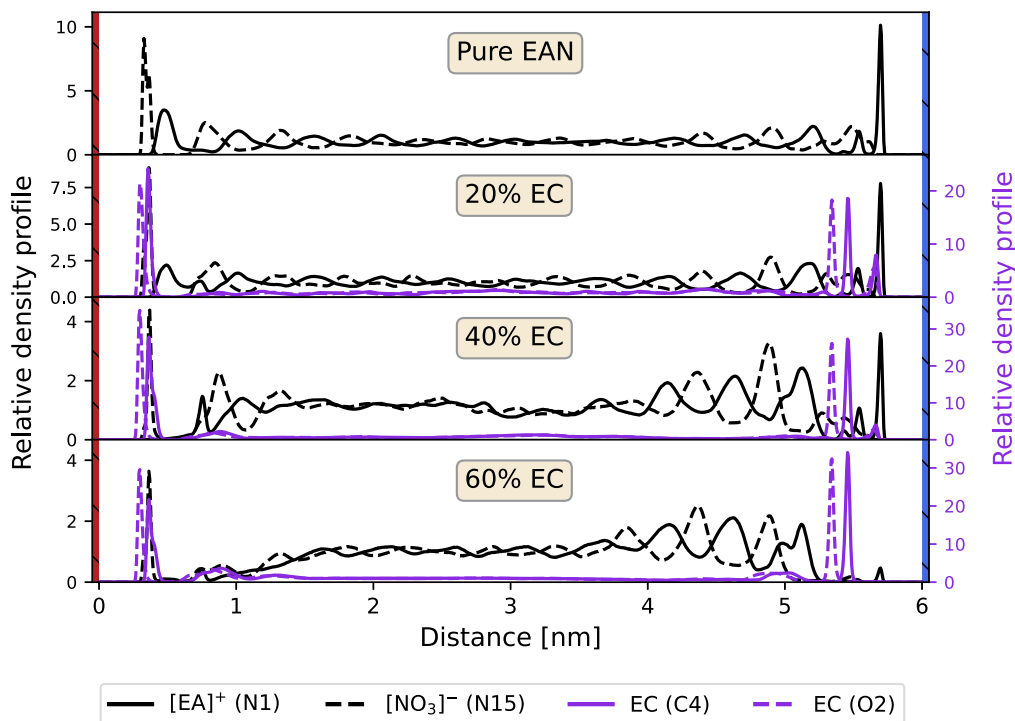
Fig. 10. Density profiles, normalized to the bulk density, for different atoms in the system at several concentrations when an electric field is applied. The atoms related to IL molecules are represented in black and those related to EC in violet. Note that the scales on the left and right *y*-axes are different, referring the former to IL atoms and the latter to EC atoms. The positive and negative walls are represented in red and blue, respectively.
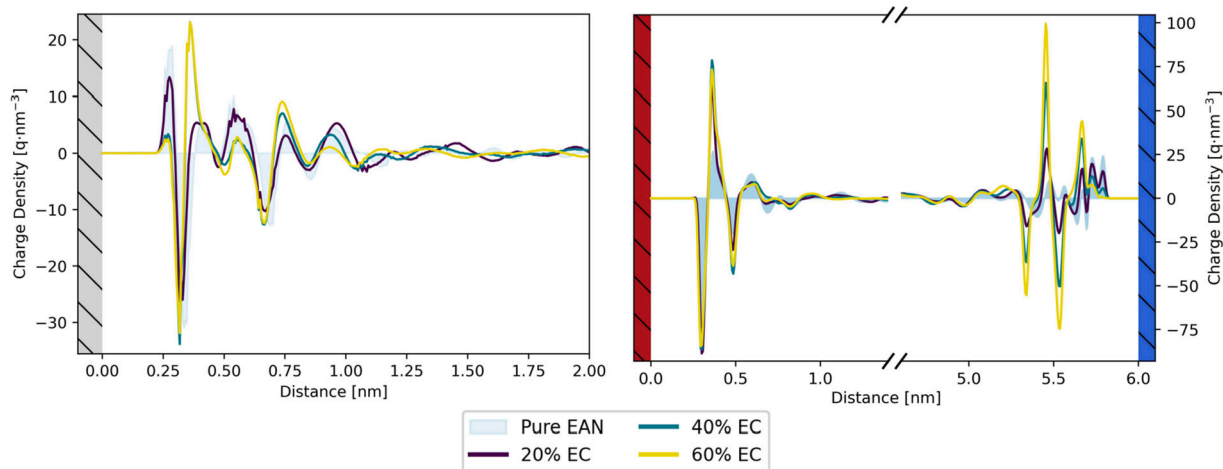

Fig. 11. Charge density profiles in the perpendicular direction to the walls at different EC concentrations for neutral (left) and charged (right) wall systems. In both cases, bulk is omitted since it oscillates around zero. For neutral walls systems the right surface is not shown due to symmetry reasons. The positive and negative walls are represented in red and blue, respectively.

3.2.2. Charge density profiles and orientations

Charge density profiles are shown in Fig. 11. For the systems between neutral carbon structures a zero charge zone is found in the middle of the nanoslit, whereas near the walls alternating positive-negative charge layers are observed due to the EDLs formation. The EC added to EAN is able to modify the charge profile in the neighborhood of the surface and provokes the excess positive charge to be displaced far from the walls, as it can be observed in the evolution of the height of the first and third peaks of the charge density when high molar fractions of solvent are reached. Apparently, the formation of these layers at such close distances to the wall seems to contradict what was analyzed in Fig. 9, where it was found that the ions (and thus the fundamental charge source of the system) were displaced by the carbonate from

this vicinity at high cosolvent concentrations. Likewise, the fact that the positive charge is accumulated in the area closest to the surfaces when there is low carbonate concentration does not seem to be compatible with the fact that the anion is the species that appears closest to the wall (Fig. 9).

To understand the reason behind this charge arrangement, it is essential to consider the orientations of the different species in the system. For this purpose, the probability of finding a molecule in the 0.7 nm-wide region from the wall forming a certain angle θ between a vector perpendicular to the walls (pointing towards the bulk) and its characteristic molecular vector was calculated. For the cation, a vector joining both carbons with the application point being the carbon further from nitrogen (C8) was used. For the anion, the vector is such that it is per-
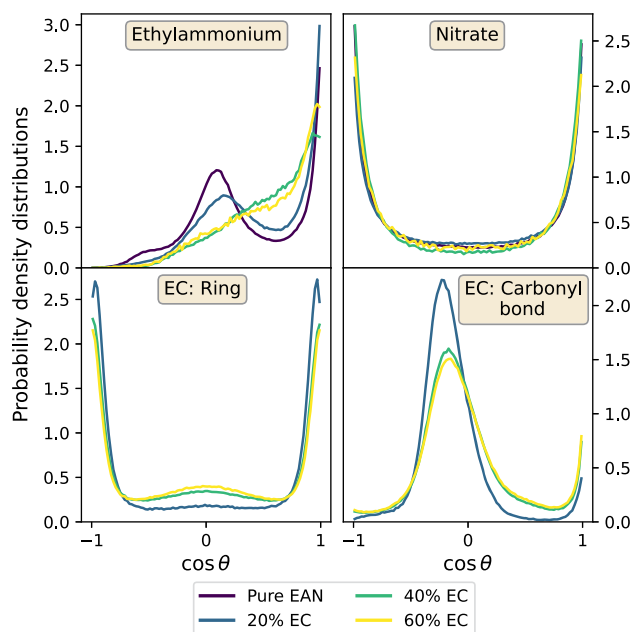
Fig. 12. Marginal probability density distributions as a function of $\cos\theta$ for the different species in the neutral walls system in the region near the wall (up to 0.7 nm).

pendicular to the plane formed by the atoms of the molecule, with its application point fixed at its center of mass. For EC two molecular vectors were taken into account: firstly, a vector normal to the ring (with the center of mass of the ring as application point) and, secondly, the vector of the carbonyl bond (with the carbon as application point). For the purpose of clarity, the characteristic vector of each molecule is represented in Fig. S5 of the Supporting Information. The marginal probability distribution of this conditional probability is shown in Fig. 12. Looking first at $[EA]^+$, this molecule is found in this region with the tail perpendicular to the surface and carbon C8 being the closest atom, especially at low EC concentrations. In this way, the tails of $[EA]^+$ are placed so that the combined partial charges of the methyl group generate the positively charged region, explaining the appearance of a positive peak at around 0.25 nm for the case of pure EAN in Fig. 11. This also explains its difference with the adjacent negative region in terms of their absolute values, since the latter is generated by the anions lying parallel to the wall. As it can be seen in Fig. 12, the increase in EC concentration makes the parallel position of the cation slightly less favored, promoting a new range of orientations. This behavior, together with $[EA]^+$ displacement from the region close to the walls, explains the fading of the positively charged zone. The explanation of why the first zone of negative excess charge does not disappear with increasing EC concentration can be found in the orientations of the cosolvent itself. Looking at both plots in the bottom row of Fig. 12, they reveal how the EC is positioned in such a way that, while keeping the ring parallel to the wall, the double bond of the carbonyl group remains so that the oxygen is closer to the surface. Since this oxygen carries the greatest partial negative charge of the entire molecule, this particular arrangement generates the charge structure that can be observed in Fig. 11 for high EC concentrations, with a first remarkable negative zone followed by a positive one. Finally, it is important to highlight the role of the cosolvent concentration in this charge distribution and in the orientations of most of the ionic species. Specifically, it can be seen that there is a radical change in trend in both cases between 20% and 40% EC concentration. This is probably due to the formation of the second layer that could be observed in Fig. 9, which marks the separation between two regimes: one with a relative strong ionic presence in the layer closest to the wall and a second where this presence is restricted to the second layer.

On the other hand, when analyzing the profile of charged walls systems in Fig. 11, two different behaviors are found depending on the surface considered. In the region around the positive wall, no appreciable change is registered when increasing EC concentration. The only notable aspect is the considerable increase in the accumulation of positive charge around 0.4 nm with the increase in EC concentration. The explanation lies in the orientation of the carbonates, specifically their double bond, which can be analyzed thanks to the oxygen and carbon density profiles that form the bond and are shown in Fig. 10. In this case, the oxygen is located pointing towards the wall and the rest of the carbonate body, in a similar way to what happened in the case of neutral walls, is found in the posterior region, thus provoking an accumulation of additional positive charge in said area that compensates the displacement of the cation. This description can be also seen when analyzing the orientations of the different species in the proximity of the positively charged surface, which are included in Fig. S6 of the Supporting Information. However, near the negative surface more significant changes are found due to the presence of carbonate. For low solvent concentrations, a double peak formation is observed in the region adjacent to the wall due to the presence of the two $[EA]^+$ layers that are present in Fig. 10. When increasing the EC concentration, this structure disappears and the typical alternate positive-negative layer profile is presented. This change is observed at the same concentrations as the change in the profile of neutral walls was found (20 and 40% EC), but more significant changes are obtained for concentrations above 40%. It is interesting to note that for the most concentrated mixture, the more relevant peaks in the charge profile are entirely due to the orientation of the EC, whose presence has completely displaced the ionic species from the interface. In this way, the closest positive excess charge is caused by the methylene groups in the ring, followed by a negative peak due to the oxygens of the ring. Then, a second positive peak due to the carbon of the carbonyl group and, finally, a negative layer created by the oxygen of that same group. As before, this is confirmed by the calculation of the orientations of the different molecules in the proximity of the negatively charged surface, which are included in Fig. S7 of the Supporting Information. It can be seen that, for both electrodes, the orientation of the co-ion and the carbonate is modified when increasing EC concentration. We expect that, if we increase the strength of the electric field, that modification would take place at higher EC concentrations, since the carbonate would have more difficulties for displacing the ionic species from the interface. Also, at high concentrations, since the ions are accumulated behind the barriers formed by the EC, the charge profiles further apart than 0.7 nm from the wall are attenuated compared to those at the interface due to a high degree of ionic pair aggregation.

4. Conclusions

The structure and dynamics of binary mixtures of a protic ionic liquid, EAN, and a carbonate solvent, EC, were studied in both bulk and interfacial situations by using MD simulations. Also experimental measurements of density and conductivity were carried out to compare with the results of such simulations. Experimental analysis revealed a solubility limit of 60% of EC at room temperature.

Computational structural analysis of bulk mixtures showed that EC is mainly located in the apolar regions of the IL, thus being unable to break the well-known hydrogen bond network formed by EAN. This resilience of the H-bond network can be also inferred from the dynamic properties, since the ionic motion is not favored up to EC concentrations close to saturation. These findings are consistent with the experimental conductivity not increasing in comparison to the pure IL with increasing the carbonate content (even showing a slightly falling tendency) due to the nonexistence of remarkable changes in the ionic environment.

Interfacial simulations with neutral walls revealed that EC presents greater affinity for the carbon surface than the IL, displacing the latter from its neighborhood and restricting it to the central region of the simulation box for high amounts of EC. Indeed there is a shift in

the behavior of the system at carbonate concentrations over 20%, from which the IL is completely displaced from the region directly next to the wall. Also, some kind of separation between the compounds can be distinguished at the highest analyzed EC concentration, which can be interpreted as the miscibility limit being reached at lower carbonate amounts than in the bulk. When an electric field is applied, it was found that nitrate anions are able to compete against EC to be placed in the region near the positively charged wall. If high concentrations of carbonate are reached, cations cannot be located close to the negatively charged surface due to their large size. Finally, the orientation of the carbonate was observed to have an effect on the charge distribution around the cations in both neutral and charged wall simulations.

On the one hand, our results seem to predict that, if ternary mixtures of EAN, EC and a metal salt are used in energy storage devices such as supercapacitors, the amount of carbonate should be lower than 20% in order to avoid this compound to impregnate the electrode (and so impeding the interaction between the metal ion and the electrode). However, a study of this kind of ternary mixtures should be carried out to properly estimate the ability of the metal cation to reach the electrode, thus confirming or disproving this hypothesis, but up to our knowledge no works combining these species can be found in the literature. On the other hand, electrode impregnation by the carbonate can be considered as a positive aspect in battery applications, since it can help the formation and stabilization of the solid electrolyte interface [71,72]. Additionally, the binary mixtures analyzed in this work could be useful in applications such as synthesis and catalysis, since EC and ILs have been already employed to produce ethylene glycol or dimethyl carbonate, but further analysis would be required.

CRediT authorship contribution statement

Raúl Lois-Cuns: Formal analysis, Investigation, Methodology, Software, Validation, Visualization, Writing – original draft, Writing – review & editing. **Martín Otero-Lema:** Formal analysis, Investigation, Methodology, Software, Validation, Visualization, Writing – review & editing. **Alejandro Rivera-Pousa:** Formal analysis, Investigation, Methodology, Software, Supervision, Validation, Visualization, Writing – review & editing. **Pablo Vallet:** Formal analysis, Investigation, Methodology, Validation, Visualization, Writing – original draft, Writing – review & editing. **Juan J. Parajó:** Formal analysis, Investigation, Methodology, Validation, Visualization, Writing – original draft, Writing – review & editing. **Oscar Cabeza:** Conceptualization, Formal analysis, Visualization, Writing – review & editing. **Hadrián Montes-Campos:** Conceptualization, Formal analysis, Investigation, Methodology, Project administration, Software, Supervision, Validation, Visualization, Writing – review & editing. **Trinidad Méndez-Morales:** Conceptualization, Formal analysis, Funding acquisition, Investigation, Methodology, Project administration, Software, Supervision, Validation, Visualization, Writing – original draft, Writing – review & editing. **Luis M. Varela:** Conceptualization, Formal analysis, Funding acquisition, Project administration, Supervision, Visualization, Writing – review & editing.

Declaration of competing interest

The authors declare that they have no known competing financial interests or personal relationships that could have appeared to influence the work reported in this paper.

Data availability

Data will be made available on request.

Acknowledgements

Appendix A. Supplementary material

Supplementary material related to this article can be found online at https://doi.org/10.1016/j.molliq.2023.122361.

References

[1] M. Galiński, A. Lewandowski, I. Stepniak, Ionic liquids as electrolytes, Electrochim. Acta 51 (2006) 5567–5580.

[2] M. Armand, F. Endres, D.R. MacFarlane, H. Ohno, B. Scrosati, Ionic-liquid materials for the electrochemical challenges of the future, Nat. Mater. 8 (2009) 621–629.

[3] H. Niu, L. Wang, P. Guan, N. Zhang, C. Yan, M. Ding, X. Guo, T. Huang, X. Hu, Recent advances in application of ionic liquids in electrolyte of lithium ion batteries, J. Energy Storage 40 (2021) 102659.

[4] P. Wasserscheid, W. Keim, Ionic liquids—new "solutions" for transition metal catalysis, Angew. Chem. Int. Ed. 39 (2000) 3772–3789.

[5] T.L. Greaves, C.J. Drummond, Protic ionic liquids: properties and applications, Chem. Rev. 108 (2008) 206–237.

[6] S. Zhang, N. Sun, X. He, X. Lu, X. Zhang, Physical properties of ionic liquids: database and evaluation, J. Phys. Chem. Ref. Data 35 (2006) 1475–1517.

[7] L.T. Le, T.D. Vo, K.H. Ngo, S. Okada, F. Alloin, A. Garg, P.M. Le, Mixing ionic liquids and ethylene carbonate as safe electrolytes for lithium-ion batteries, J. Mol. Liq. 271 (2018) 769–777.

[8] A. Guerfi, M. Dontigny, P. Charest, M. Petitclerc, M. Lagacé, A. Vijh, K. Zaghib, Improved electrolytes for Li-ion batteries: mixtures of ionic liquid and organic electrolyte with enhanced safety and electrochemical performance, J. Power Sources 195 (2010) 845–852.

[9] A. Krause, A. Balducci, High voltage electrochemical double layer capacitor containing mixtures of ionic liquids and organic carbonate as electrolytes, Electrochem. Commun. 13 (2011) 814–817.

[10] T. Vogl, S. Menne, A. Balducci, Mixtures of protic ionic liquids and propylene carbonate as advanced electrolytes for lithium-ion batteries, Phys. Chem. Chem. Phys. 16 (2014) 25014–25023.

[11] B. Ghalami-Choobar, T.N. Fallahkar, Thermophysical properties of 1-ethyl-3-methylimidazolium bromide ionic liquid in water+ ethylene carbonate mixtures at T = (298.2, 308.2 and 318.2) K, Fluid Phase Equilib. 496 (2019) 42–60.

[12] A. Brandt, C. Ramirez-Castro, M. Anouti, A. Balducci, An investigation about the use of mixtures of sulfonium-based ionic liquids and propylene carbonate as electrolytes for supercapacitors, J. Mater. Chem. A 1 (2013) 12669–12678.

[13] Y.-J. Kim, Y. Matsuzawa, S. Ozaki, K.C. Park, C. Kim, M. Endo, H. Yoshida, G. Masuda, T. Sato, M.S. Dresselhaus, High energy-density capacitor based on ammonium salt type ionic liquids and their mixing effect by propylene carbonate, J. Electrochem. Soc. 152 (2005) A710.

[14] A. Stoppa, J. Hunger, R. Buchner, Conductivities of binary mixtures of ionic liquids with polar solvents, J. Chem. Eng. Data 54 (2009) 472–479.

[15] L. Xu, X. Cui, Y. Zhang, T. Feng, R. Lin, X. Li, H. Jie, Measurement and correlation of electrical conductivity of ionic liquid [EMIM][DCA] in propylene carbonate and γ-butyrolactone, Electrochim. Acta 174 (2015) 900–907.

[16] Q.-G. Zhang, S.-S. Sun, S. Pitula, Q.-S. Liu, U. Welz-Biermann, J.-J. Zhang, Electrical conductivity of solutions of ionic liquids with methanol, ethanol, acetonitrile, and propylene carbonate, J. Chem. Eng. Data 56 (2011) 4659–4664.

[17] R. Zarrougui, M. Dhahbi, D. Lemordant, Effect of temperature and composition on the transport and thermodynamic properties of binary mixtures of ionic liquid n-butyl-n-methylpyrrolidinium bis (trifluoromethanesulfonyl) imide and propylene carbonate, J. Solution Chem. 39 (2010) 921–942.

[18] N. Salem, Y. Abu-Lebdeh, Non-flammable electrolyte mixtures of ringed ammonium-based ionic liquids and ethylene carbonate for high voltage Li-ion batteries, J. Electrochem. Soc. 161 (2014) A1593.

[19] J. Pires, L. Timperman, J. Jacquemin, A. Balducci, M. Anouti, Density, conductivity, viscosity, and excess properties of (pyrrolidinium nitrate-based protic ionic liquid+propylene carbonate) binary mixture, J. Chem. Thermodyn. 59 (2013) 10–19.

[20] S. Pohlmann, T. Olyschläger, P. Goodrich, J.A. Vicente, J. Jacquemin, A. Balducci, Mixtures of azepanium based ionic liquids and propylene carbonate as high voltage electrolytes for supercapacitors, Electrochim. Acta 153 (2015) 426–432.

[21] R.A. Di Leo, A.C. Marschilok, K.J. Takeuchi, E.S. Takeuchi, Battery electrolytes based on saturated ring ionic liquids: physical and electrochemical properties, Electrochim. Acta 109 (2013) 27–32.

[22] K. Fayyaz, S. Jafary, P. Bakhshi, M. Madani, Accurate prediction of electrical conductivity of ionic liquids+ propylene carbonate binary mixtures, J. Mol. Liq. 279 (2019) 400–410.

[23] N. Zec, A. Idrissi, M. Bešter-Rogač, M. Vraneš, S. Gadžurić, Insights into interactions between 1-butyl-3-methylimidazolium dicyanamide and molecular solvents: γ-valerolactone, γ-butyrolactone and propylene carbonate. Volumetric properties and MD simulations, J. Mol. Liq. 268 (2018) 481–489.

[24] S.W. Coles, A.M. Smith, M.V. Fedorov, F. Hausen, S. Perkin, Interfacial structure and structural forces in mixtures of ionic liquid with a polar solvent, Faraday Discuss. 206 (2018) 427–442.

[25] R.-S. Kühnel, N. Böckenfeld, S. Passerini, M. Winter, A. Balducci, Mixtures of ionic liquid and organic carbonate as electrolyte with improved safety and performance for rechargeable lithium batteries, Electrochim. Acta 56 (2011) 4092–4099.

[26] E. Bolimowska, F. Castiglione, J. Devemy, H. Rouault, A. Mele, A.A. Pádua, C.C. Santini, Investigation of Li⁺ cation coordination and transportation, by molecular modeling and nmr studies, in a LiNTf₂-doped ionic liquid–vinylene carbonate mixture, J. Phys. Chem. B 122 (2018) 8560–8569.

[27] B. Gélinas, M. Natali, T. Bibienne, Q.P. Li, M. Dollé, D. Rochefort, Electrochemical and transport properties of ions in mixtures of electroactive ionic liquid and propylene carbonate with a lithium salt for lithium-ion batteries, J. Phys. Chem. C 120 (2016) 5315–5325.

[28] R.-S. Kühnel, A. Balducci, Lithium ion transport and solvation in n-butyl-n-methylpyrrolidinium bis (trifluoromethanesulfonyl) imide–propylene carbonate mixtures, J. Phys. Chem. C 118 (2014) 5742–5748.

[29] K. Oldiges, D. Diddens, M. Ebrahiminia, J. Hooper, I. Cekic-Laskovic, A. Heuer, D. Bedrov, M. Winter, G. Brunklaus, Understanding transport mechanisms in ionic liquid/carbonate solvent electrolyte blends, Phys. Chem. Chem. Phys. 20 (2018) 16579–16591.

[30] B. Ghalami-Choobar, T. Nosrati Fallahkar, Conductometric and refractometric studies of 1-propyl-3-methylimidazolium bromide ionic liquid in water+ethylene carbonate mixtures at T=(298.2, 308.2 and 318.2) K, Phys. Chem. Res. 8 (2020) 429–455.

[31] T. Vo, H. Nguyen, Q. Nguyen, Q. Phung, V. Tran, P. Le, Carbonate solvents and ionic liquid mixtures as an electrolyte to improve cell safety in sodium-ion batteries, J. Chem. (2019) 2019.

[32] N. Dupré, P. Moreau, E. De Vito, L. Quazuguel, M. Boniface, H. Kren, P. Bayle-Guillemaud, D. Guyomard, Carbonate and ionic liquid mixes as electrolytes to modify interphases and improve cell safety in silicon-based Li-ion batteries, Chem. Mater. 29 (2017) 8132–8146.

[33] A. Deshpande, L. Kariyawasam, P. Dutta, S. Banerjee, Enhancement of lithium ion mobility in ionic liquid electrolytes in presence of additives, J. Phys. Chem. C 117 (2013) 25343–25351.

[34] Z. Li, O. Borodin, G.D. Smith, D. Bedrov, Effect of organic solvents on Li⁺ ion solvation and transport in ionic liquid electrolytes: a molecular dynamics simulation study, J. Phys. Chem. B 119 (2015) 3085–3096.

[35] M.S. Miran, H. Kinoshita, T. Yasuda, M.A.B.H. Susan, M. Watanabe, Hydrogen bonds in protic ionic liquids and their correlation with physicochemical properties, Chem. Commun. 47 (2011) 12676–12678.

[36] S. Zhang, J. Zhang, Y. Zhang, Y. Deng, Nanoconfined ionic liquids, Chem. Rev. 117 (2017) 6755–6833.

[37] P. Vallet, S. Bouzón-Capelo, T. Méndez-Morales, V. Gómez-González, Y. Arosa, R. de la Fuente, E. López-Lago, J.R. Rodríguez, L.J. Gallego, J.J. Parajó, et al., On the physical properties of mixtures of nitrate salts and protic ionic liquids, J. Mol. Liq. 350 (2022) 118483.

[38] V. Pokorný, V. Štejfa, M. Fulem, C. Červinka, K. Růžička, Vapor pressures and thermophysical properties of ethylene carbonate, propylene carbonate, γ-valerolactone, and γ-butyrolactone, J. Chem. Eng. Data 62 (2017) 4174–4186.

[39] J. Salgado, J. Parajó, M. Villanueva, J. Rodríguez, O. Cabeza, L. Varela, Liquid range of ionic liquid – metal salt mixtures for electrochemical applications, J. Chem. Thermodyn. 134 (2019) 164–174.

[40] Abraham Lindahl, Spoel van der Hess, GROMACS 2019.5 source code, https://doi.org/10.5281/zenodo.3577986, 2019.

[41] M.J. Abraham, T. Murtola, R. Schulz, S. Páll, J.C. Smith, B. Hess, E. Lindahl, GROMACS: high performance molecular simulations through multi-level parallelism from laptops to supercomputers, SoftwareX 1 (2015) 19–25.

[42] D. Van Der Spoel, E. Lindahl, B. Hess, G. Groenhof, A.E. Mark, H.J. Berendsen, GROMACS: fast, flexible, and free, J. Comput. Chem. 26 (2005) 1701–1718.

[43] W.L. Jorgensen, J. Tirado-Rives, The OPLS [optimized potentials for liquid simulations] potential functions for proteins, energy minimizations for crystals of cyclic peptides and crambin, J. Am. Chem. Soc. 110 (1988) 1657–1666.

[44] W.L. Jorgensen, D.S. Maxwell, J. Tirado-Rives, Development and testing of the OPLS all-atom force field on conformational energetics and properties of organic liquids, J. Am. Chem. Soc. 118 (1996) 11225–11236.

[45] S.V. Sambasivarao, O. Acevedo, Development of opls-aa force field parameters for 68 unique ionic liquids, J. Chem. Theory Comput. 5 (2009) 1038–1050.

[46] X. You, M.I. Chaudhari, S.B. Rempe, L.R. Pratt, Dielectric relaxation of ethylene carbonate and propylene carbonate from molecular dynamics simulations, J. Phys. Chem. B 120 (2016) 1849–1853.

[47] B. Docampo-Álvarez, V. Gómez-González, T. Méndez-Morales, J. Carrete, J.R. Rodríguez, O. Cabeza, L.J. Gallego, L.M. Varela, Mixtures of protic ionic liquids and molecular cosolvents: a molecular dynamics simulation, J. Chem. Phys. 140 (2014) 214502.

[48] J.M. Otero-Mato, H. Montes-Campos, O. Cabeza, L.J. Gallego, L.M. Varela, Nanoconfined ionic liquids: a computational study, J. Mol. Liq. 320 (2020) 114446.

[49] L. Martínez, R. Andrade, E.G. Birgin, J.M. Martínez, Packmol: a package for building initial configurations for molecular dynamics simulations, J. Comput. Chem. 30 (2009) 2157–2164.

[50] U. Essmann, L. Perera, M.L. Berkowitz, T. Darden, H. Lee, L.G. Pedersen, A smooth particle mesh Ewald method, J. Chem. Phys. 103 (1995) 8577–8593.

[51] B. Hess, H. Bekker, H.J.C. Berendsen, J.G.E.M. Fraaije, Lincs: a linear constraint solver for molecular simulations, J. Comput. Chem. 18 (1997) 1463–1472.

[52] B. Hess, P-lincs: a parallel linear constraint solver for molecular simulation, J. Chem. Theory Comput. 4 (2007) 116–122.

[53] I.-C. Yeh, M.L. Berkowitz, Ewald summation for systems with slab geometry, J. Chem. Phys. 111 (1999) 3155–3162.

[54] G. Bussi, D. Donadio, M. Parrinello, Canonical sampling through velocity rescaling, J. Chem. Phys. 126 (2007) 014101.

[55] M. Parrinello, A. Rahman, Polymorphic transitions in single crystals: a new molecular dynamics method, J. Appl. Phys. 52 (1981) 7182–7190.

[56] D. Ausín, J.J. Parajó, J.L. Trenzado, L.M. Varela, O. Cabeza, L. Segade, Influence of small quantities of water on the physical properties of alkylammonium nitrate ionic liquids, Int. J. Mol. Sci. 22 (2021).

[57] M. Haughney, M. Ferrario, I.R. McDonald, Molecular-dynamics simulation of liquid methanol, J. Phys. Chem. 91 (1987) 4934–4940.

[58] K. Fumino, A. Wulf, R. Ludwig, Hydrogen bonding in protic ionic liquids: reminiscent of water, Angew. Chem. Int. Ed. 48 (2009) 3184–3186.

[59] R.J. Gowers, P. Carbone, A multiscale approach to model hydrogen bonding: the case of polyamide, J. Chem. Phys. 142 (2015) 224907.

[60] P. Martínez-Crespo, M. Otero-Lema, O. Cabeza, H. Montes-Campos, L.M. Varela, Structure, dynamics and ionic conductivities of ternary ionic liquid/lithium salt/DMSO mixtures, J. Mol. Liq. 359 (2022) 119188.

[61] R. Zarrougui, M. Dhahbi, D. Lemordant, Transport and thermodynamic properties of ethylammonium nitrate–water binary mixtures: effect of temperature and composition, J. Solution Chem. 44 (2015) 686–702.

[62] A. Nazet, L. Weiß, R. Buchner, Dielectric relaxation of nitromethane and its mixtures with ethylammonium nitrate: evidence for strong ion association induced by hydrogen bonding, J. Mol. Liq. 228 (2017) 81–90.

[63] Y. Litaiem, M. Dhahbi, Measurements and correlation of viscosity and conductivity for the mixtures of ethylammonium nitrate with organic solvents, J. Mol. Liq. 155 (2010) 42–50.

[64] O. Borodin, Polarizable force field development and molecular dynamics simulations of ionic liquids, J. Phys. Chem. B 113 (2009) 11463–11478.

[65] K. Goloviznina, J.N. Canongia Lopes, M. Costa Gomes, A.A. Pádua, Transferable, polarizable force field for ionic liquids, J. Chem. Theory Comput. 15 (2019) 5858–5871.

[66] J.M. Otero-Mato, H. Montes-Campos, V. Gómez-González, M. Montoto, O. Cabeza, S. Kondrat, L.M. Varela, Structure, dynamics and conductivities of ionic liquid-alcohol mixtures, J. Mol. Liq. 355 (2022) 118955.

[67] T. Yu, Q. Cai, G. Lian, L. Liu, Molecular dynamics studies on separation of co2/ch4 by the ionic liquids encapsulated zif-8, J. Membr. Sci. 644 (2022) 120117.

[68] M.V. Fedorov, A.A. Kornyshev, Towards understanding the structure and capacitance of electrical double layer in ionic liquids, Electrochim. Acta 53 (2008) 6835–6840.

[69] M.Z. Bazant, B.D. Storey, A.A. Kornyshev, Double layer in ionic liquids: overscreening versus crowding, Phys. Rev. Lett. 106 (2011) 046102.

[70] A. Kornyshev, Double-layer in ionic liquids: paradigm change?, J. Phys. Chem. B 117 (2013) 13946.

[71] L. Xing, X. Zheng, M. Schroeder, J. Alvarado, A. von Wald Cresce, K. Xu, Q. Li, W. Li, Deciphering the ethylene carbonate–propylene carbonate mystery in Li-ion batteries, Acc. Chem. Res. 51 (2018) 282–289.

[72] T. Melin, R. Lundström, E.J. Berg, Revisiting the ethylene carbonate–propylene carbonate mystery with operando characterization, Adv. Mater. Interfaces 9 (2022) 2101258.